Environmental Science: Atmospheres

ROYAL SOCIETY OF CHEMISTRY

PAPER

View Article Online
View Journal | View Issue

Cite this: *Environ. Sci.: Atmos.*, 2024, **4**, 1266

Trace elements in $PM_{2.5}$ shed light on Saharan dust incursions over the Munich airshed in spring 2022†

Sara Padoan,*[a] Alessandro Zappi,[b] Jan Bendl,[a] Tanja Herrmann,[a] Ajit Mudan,[a] Carsten Neukirchen,[a] Erika Brattich,[c] Laura Tositti[b] and Thomas Adam *[a]

Received 27th June 2024
Accepted 25th September 2024

DOI: 10.1039/d4ea00092g

rsc.li/esatmospheres

The influence of a prolonged Saharan Dust event across Europe and specifically in Munich (Germany) in March 2022 was detected and analyzed in detail. The event arose from a sequence of Saharan Dust incursions intertwined with a stagnation in the regional circulation leading to the persistence of a mineral dust plume for several weeks over the region. Trace element and meteorological data were collected. Enrichment factors, size distribution analyses, and multivariate techniques such as Varimax and Self-Organizing Maps (SOM) were applied to highlight the influence of Saharan Dusts and to evaluate the pollution sources in Munich municipality. The overall results revealed how the Munich airshed was clearly affected by long-distance mineral dusts from the North African desert, that increased the concentrations of natural (*e.g.* Al, Mg, Ca) and anthropogenic (*e.g.* Sb, Mo, Pb) elements based on the different paths followed by the dusts. Moreover, the chemometric analyses revealed a range of well-defined local anthropogenic emission sources including road traffic, energy production by coal combustion (S and Se), traffic (Cu, Sb), and waste incineration (Zn).

Environmental significance

Trace elements (TE) in particulate matter (PM) are markers of several human activities and natural events. Analysis and quantification of TE allow the evaluation of pollution sources in the examined area, ranging from Saharan dust transport to road traffic and waste incinerator activities. Statistical analyses are very powerful tools to improve the knowledge made accessible by TE analysis. For the present work, TE in $PM_{2.5}$ samples were quantified in the Munich airshed and the TE concentrations were elaborated by self-organizing map (SOM) analysis. By SOM, the major pollution sources in Munich were disclosed, and two Saharan dust events were studied in detail.

1. Introduction

Currently, the long-range transport (LRT) of dust from deserts is widely recognized to have a significant impact on air quality across the European continent.[1–6] The world's largest source of mineral dust is the Sahara Desert, which is widely acknowledged to produce more than half of the world's geogenic particulate matter (PM).[7] Mineral dust originates from the continuous wind erosion of soil in arid regions.[8] The mechanisms responsible for mineral dust resuspension and remobilization are still objects of research owing to their complexities.[9,10] Routes and frequencies of such LRT Saharan Dust (LRT-SD) events have been closely monitored for a long time.[11] As a result, while in the past LRT-SD events mainly reached the southern part of Europe, nowadays SD outbursts may reach higher latitudes more frequently, and with increasing intensity,[2,12,13] with direct and indirect consequences on both human health and ecosystems.[5,14–17] Remarkably, SD outbursts have been found to increase in frequency[12] and to extend their influence on a wider area than the Mediterranean basin with events often crossing the Alps and reaching even the UK and Iceland.[18] Such modifications have been associated with climate change and anthropogenic forcing.[19] From the climatic point of view, tropospheric dust particles may produce direct effects on the atmospheric radiative balance by scattering and absorbing solar radiation, and indirectly by affecting cloud microphysics and the likelihood of precipitation by formation of cloud condensation nuclei.[20] At the ground level, SD can lead PM to exceed air quality standards according to Directive 2008/50/EC,[21] though these events could be discarded from the dataset of pollution-related exceedances, as they are caused by natural events. Recent literature, however, has pointed out that

[a]*University of the Bundeswehr Munich, Faculty for Mechanical Engineering, Institute of Chemistry and Environmental Engineering, Werner-Heisenberg-Weg 39, 85577, Neubiberg, Germany. E-mail: sara.padoan@unibw.de; jan.bendl@unibw.de; tanja.pern@gmx.de; m61bajmu@unibw.de; carsten.neukirchen@unibw.de; sarina199125@gmail.com; thomas.adam@unibw.de; Tel: +49 89 6004 4649*

[b]*University of Bologna, Department of Chemistry "G. Ciamician", Via Selmi 2, 40126, Bologna, Italy. E-mail: alessandro.zappi4@unibo.it; laura.tositti@unibo.it*

[c]*University of Bologna, Department of Physics and Astronomy "Augusto Righi", Via Irnerio 46, 40126, Bologna, Italy. E-mail: erika.brattich@unibo.it*

† Electronic supplementary information (ESI) available. See DOI: https://doi.org/10.1039/d4ea00092g

mineral dust too is associated with toxic effects on human health deserving attention and monitoring.[22–26]

What is described above thus suggests that more attention needs to be paid to this type of aerosol source. Its contribution to a local aerosol mixture might not only affect mass load but also atmospheric chemistry with cascade effects on the environment and human health. In fact, besides their intrinsic toxicity, SD particles can interact with reactive precursor gases of local origin, as well as with other types of particles. Such interactions are mediated by local circulation and mixing, possibly contributing to the deterioration of environmental conditions at the local scale.[27]

In this framework, SD incursions into Germany have already been detected before.[13,28,29] The present study reports the result of a survey based on major and trace elements (TE) in $PM_{2.5}$ samples collected during a spring campaign in 2022 in the town of Neubiberg, which is located at the south-eastern outskirts of Munich, Germany. Results revealed that the receptor site is affected by several PM sources, both from the district and influenced by large-scale and prolonged SD transport over Europe. The presence of such events was widely reported internationally by the media and confirmed by remote sensing data (*e.g.* from EU Copernicus satellite observation[30]). The results obtained in this study were combined with optical particle sizer data, meteorological data, and back-trajectory analyses to investigate the association of PM source profiles with the transport of desert dust in the local airsheds.

In particular, as an alternative to source apportionment methods, a chemometric analysis based on self-organizing maps (SOM)[31] was applied to describe the effect of SD events on the Munich airshed. The SOM method is gaining attention in environmental studies[32] owing to its ability to process data that are unsuitable for other source apportionment methodologies, such as positive matrix factorization.[33] Additionally, this method allows for easy interpretation of results and assessment of variables' relationships. Therefore, the use of SOM allowed not only the presence and the effects of SD to be evaluated but also a first source apportionment analysis of Munich trace-element pollution to be performed.

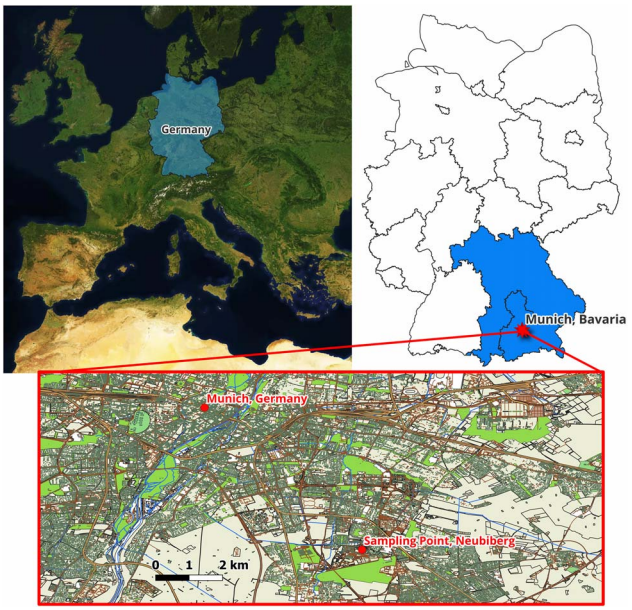

Fig. 1 Sampling area, campus of UniBwM at Neubiberg, Germany.

2. Materials and methods

2.1. Studied area, PM sampling, and measurements

The city of Munich with a population of *ca.* 1.5 million is part of the Northern Alpine Foreland at an average altitude of 520 m a.s.l. It has a marine west coast climate (Cfb) according to the Köppen Climate Classification. The sampling site is located inside the campus of the University of the Bundeswehr Munich (UniBwM; 48.0771 N, 11.6393 E) in the municipality of Neubiberg, which is bordering the city of Munich to the south-east, and which is about 50 km north of the Alps. Fig. 1 shows a map of the sampling area, created with QGIS v.3.34.1 software.[34]

This work covers the sampling period from March 10th to May 11th 2022 and is part of the long-term measurement campaign within the Munich Mobility Research Campus (MORE) project (**https://www.unibw.de/more**). During this period, two SD events were registered lasting from March 14th to 18th and from March 27th to 30th, as confirmed by Copernicus satellite observation. Sixty $PM_{2.5}$ samples were collected daily over 24 h (start/end at 9:00 am) using a high-volume sampler (DHA-80, Digitel) at a flow rate of 30 $m^3\ h^{-1}$. Simultaneously, aerosol size distribution was measured online with an optical spectrometer with 1 min resolution. Temperature, air pressure, air humidity, and wind speed/direction, as well as solar and UV radiation were recorded every 10 min with a meteorological station (Vantage Pro 2, Davis) on site. The closest station of the German Meteorological Service (Deutscher Wetterdienst, DWD) is located in Oberhaching-Laufzorn (48.0131 N, 11.5525 E), which is at a distance of *ca.* 9.5 km from the UniBwM campus. Temperature, humidity, and precipitation data from this DWD site were highly comparable with those from the UniBwM weather station.

2.2. Filter preparation and ICP-MS analysis

$PM_{2.5}$ samples were collected on a 150 mm quartz fiber filter (Whatman QMA, pre-conditioned for 5 h at 500 °C). From each sample, a 47 mm punch was cut out of the whole filter for analysis. Subsequently, samples were digested according to the method DIN EN 14902 in a Berghof-Microwave Digester-Speedwave Entry with a mixture of 8 mL of nitric acid (HNO_3, ultrapure grade, 69%), 2 mL of hydrogen peroxide (H_2O_2, ultrapure grade 30%) and 10 µL (to obtain a final concentration of 20 $\mu g\ L^{-1}$) of internal standard. The internal standard is added manually to each individual vessel together with the reagents and the filter sample before the digestion, allowing specific contaminations or losses during the extraction procedure to be assessed. The internal standard used is from Agilent Technologies (ICP-MS Internal Std Mix, p/n 5188-6525), containing 100 $\mu g\ mL^{-1}$ Bi, Ge, In, ^{6}Li, Lu, Rh, Sc, and Tb. Digested

samples were diluted to a final volume of 50 mL, centrifuged, and then filtered through a 0.2 μm syringe filter.

Elemental analysis was carried out with an Agilent 8900 Triple Quadrupole ICP-MS. Samples were quantified using an external calibration line from 1 μg L^{-1} to 320 μg L^{-1}. The ICP-MS standards of aluminum (Al), arsenic (As), barium (Ba), cadmium (Cd), chromium (Cr), copper (Cu), manganese (Mn), molybdenum (Mo), nickel (Ni), lead (Pb), antimony (Sb), selenium (Se), vanadium (V) and zinc (Zn) had concentrations of 10 μg mL^{-1} and for calcium (Ca), iron (Fe), potassium (K), magnesium (Mg) and sodium (Na) of 1000 μg mL^{-1} in a matrix of 5% HNO_3. Three replicates for each sample were analyzed and the mean value was considered for data analysis. One quality control standard (consisting of a 100 μg mL^{-1} standard of all elements) was injected after the analysis of every ten samples to guarantee the method's reliability. The signal-to-noise ratio (SNR) was determined based on the calibration curves and background equivalent concentrations (BEC) were calculated. BEC was calculated as the blank value expressed in concentration units. The "blank" considered in this case is the solution used for digestion (HNO_3 and H_2O_2). Normally, it is directly calculated by the instrument software by dividing the signal in counts/second (c per s) by the slope of the calibration curve. SNR was also directly calculated by the instrument software as 3 × standard-deviations of BEC.

The limit of detection (LOD) was calculated as BEC + SNR and the limit of quantification (LOQ) was calculated as BEC + 3.33 × SNR. SNRs, BECs, LODs, and LOQs are reported in Table S1.†

Quality control solutions (QCs) were prepared and measured repeatedly and independently from calibration solutions to monitor the performance of the analysis. A QC mixed solution was prepared with different concentrations for the different elements. Na, Mg, K, Ca, and Fe had concentrations of 10 000 μg L^{-1}, Sr had a concentration of 1000 μg L^{-1} and Al, S, V, Mn, Co, Ni, Cu, Zn, As, Se, Mo, Cd, Sb, Ba, and Pb had concentrations of 100 μg L^{-1}. QC-plot control chart and statistical evaluations always showed a correct measurement of the QC solution ensuring a trustable performance of the analysis method. The same analyses were carried out with a second Agilent 7700 ICP-MS instrument for an internal intercomparison (results not shown). With this second instrument, we also analyzed three different NIST reference materials SRM-1649, ERM-CZ-100, and SRM-2975. The results are reported in Cao *et al.*, 2021.[35] Once the measurements of the environmental samples on both systems were completed, they were checked with an element-by-element *t*-test for comparability. More than 70% of the data determined with both instruments were comparable at the 95% confidence level (*p*-values < 0.05), indicating acceptable agreement between experimental and internal uncertainty.

Final data obtained from the instrumental measurement were subtracted for the respective field blanks.

2.3. SEM-EDX analysis

Two PM samples for the scanning electron microscopy with energy dispersive X-ray spectroscopy (SEM-EDX) analysis were collected passively throughout the SD events on a metal plate from which mostly coarse SD particles were carefully transferred to EDX-suitable adhesive carbon pads by pressing the pad on the metal plate.

Sedimented coarse particles of SD were transferred on ultrapure EDX-suitable adhesive carbon pads, which were transferred to 12 mm SEM pin stub sample holders. Samples were stored under vacuum for 24 h prior to their analysis to ensure removal of the volatile compounds.

Particles were imaged with the Inlens detector of a Gemini SEM 360 from Carl Zeiss (Oberkochen, Germany). EDX Analysis was conducted with an Ultim Max 40 EDX detector from Oxford Instruments (Abingdon, England) at an electron high tension (EHT) voltage of 12 kV and an optimum detector working distance of 8.5 mm. The usage of a silicon drift detector with a thin detector window ensured suitability for the analysis of low-*Z* elements ($Z > 6$) such as C and O.

2.4. Optical particle counting and mass load data

In the period 1st March–31st May aerosol size-distribution measurements at 1 min time resolution were determined using the Optical Particle Spectrometer (OPS) APDA-372 (Horiba) with an Intelligent Aerosol Drying System (IADC) and Sigma-2 sampling head. This monitor is approved for simultaneous monitoring of PM_{10} and $PM_{2.5}$ according to standards VDI 4202-1, VDI 4203-3, EN 12341, EN 14907, and EN 16450, and the EU Equivalence Guide GDE and certified in compliance with standards EN 15267-1 and -2.[36] Standard 1.3 g cm^{-3} particle density was used for calculation of aerosol mass concentration.[37] Counts of APDA-372 size bins were summed to calculate the following size distribution of PM: "fr0.2" (bin size 0.15–0.2 μm); "fr0.3" (0.2–0.3 μm); "fr0.4" (0.3–0.4 μm); "fr0.5" (0.4–0.5 μm); "fr0.6" (0.5–0.6 μm); "fr0.7" (0.6–0.7 μm); "fr0.8" (0.7–0.8 μm); "fr0.9" (0.8–0.9 μm); "fr1" (0.9–1.0 μm); "fr3" (1.0–3.0 μm); "fr5" (3.0–5.0 μm); "fr10" (5.0–10.0 μm); "fr30" (10.0 μm to the last bin, namely 26.4 μm).

OPS data were mediated over 30 min intervals in order to match with UniBwM's weather station data deployed at the receptor site. OPS data were further daily averaged to match elemental data to perform cross-correlation and multivariate analysis.

2.5. Data treatment

In order to extract the maximum information from the dataset and assess the impact of the two SD events on the composition of the $PM_{2.5}$, data were analyzed with several chemometric methods. All computations were carried out in the R 4.3.2 environment (R Core Team, Vienna, Austria). The package openair[38] was used for visual evaluation of data.

2.5.1. Enrichment factors. Prior to rigorous chemometric analysis, elemental concentration data were subjected to a preliminary evaluation using an empirical approach widely used in this field, based on the enrichment factor and diagnostic concentration ratios.[39] Enrichment factors (EF) were calculated with respect to the overall mean crustal

compositions[40] considering Al as the normalizing reference element,[41,42] using eqn (1):[43]

$$EF_X = (X/Al)_{sample}/(X/Al)_{soil} \quad (1)$$

where X is the concentration of the Xth element and the soil values were obtained from the work of Wedepohl.[40] The use of EFs is helpful as a screening tool at the beginning of a source apportionment data analysis. Indeed, these enable independent evaluations useful to consolidate source identification diagnosis. However, care is required in their use, especially in the case of man-made TE, owing to technological development shifting from older to newer processes and emissions.

2.5.2. Self-organizing maps. The most extended multivariate description of the data was carried out by Self-Organizing Maps (SOM).[31,44] SOM algorithm is an iterative grouping method that assigns each observation of the dataset to a specific unit (best matching unit, or node) based on the similarity between observations. The graphical output of SOM is a map reporting the calculated units from which information about observations and variable distributions can be extracted (*e.g.* samples assigned to the same unit have similar characteristics and close units in the map share similar properties). The computation is initialized once the number of units and the map size are decided. In the present case, we used a rectangular geometry with dimensions proportional to the two highest eigenvalues of a principal component analysis (PCA)[45] model computed on the dataset, as described in Nakagawa *et al.* (2020).[46] Thereafter, the algorithm assigns casual values to the units (that are vectors with lengths equal to the number of variables of the dataset) and presents each observation to each unit assigning it to the closest one (the best matching unit). After the first cycle, all unit vectors are updated as the mean of the assigned observations and the computation starts again. The process is iterated until convergence is reached or after a pre-defined number of cycles (epochs) are performed. SOM units can be further clustered to highlight specific properties or events described by more than one unit. The *k*-means algorithm included in the SOMEnv routine was used for the scope. This approach allows the best number of clusters to be computed based on the minimization of the Davies–Bouldin (DB) index.[47] At the end of the computation, a mean value for each variable is computed for each cluster. To better describe the behavior of variables compared to the general mean, a Wilcoxon–Mann–Whitney test was applied comparing each variable of the full dataset with the corresponding one in each cluster. All SOM computations were carried out using the R package SOMEnv.[48]

2.5.3. Back-trajectory and synoptic analysis. Back-trajectories were also calculated to evaluate the origin area of the two SD events. 120 h back-trajectories were computed using the Hybrid Single-Particle Lagrangian Integrated Trajectory (HYSPLIT_4) model[49,50] starting from the sampling point and lasting for the entire sampling period (1st March 00:00 UTC–15th May 00:00 UTC). Computations were carried out every 6 h using GFS meteorological data at 0.25° (27.8 km) resolution.[51] Four heights were considered in back-trajectory computations: 100 m, 500 m, 1000 m, and 2000 m. We used these heights because 100 m and 500 m are below the boundary layer, the first one during the entire day, and the second one only during the morning. The heights of 1000 m and 2000 m are better representatives of high-altitude transport and better explain LRT including the ones from the Sahara Desert.

Analysis of back-trajectories was further complemented with a detailed analysis of the synoptic situation based on geopotential height maps from the Zentralstadt für Meteorologie (ZAMG, Austria) and maps from the CAMS reanalysis dataset. Besides this, the analysis was supported by the visual inspection of maps from the multimodel forecast of aerosol optical depth provided by the SDS-WAS from AEMET and the Barcelona Dust Center and of vertical profiles of the attenuated back-scatter coefficient from a lidar ceilometer located in Hohenpeissenber nearby Munich. The investigation of this parameter provides an indication of the aerosol vertical profile height and thickness.

2.5.4. Varimax analysis. A further explorative analysis was carried out by Varimax,[52] an extension of PCA that rotates the principal components to obtain factors. Such factors can be used to describe the common source of the species whose loadings assume high absolute values. The optimal number of factors is chosen based on the Explained Variance (EV), which is the quantity of information retained by each factor: all factors carrying at least 5% of EV are considered significant and kept in the final model. This method proved to be a valid alternative to more efficient source apportionment methods (such as positive matrix factorization) when the size of the dataset is small.[53] Varimax analysis was carried out with the software CAT[54] based on the R 3.1.2 environment (R Core Team, Vienna, Austria).

3. Results and discussion

Due to the interconnections between the chemometric results presented in the following Paragraphs, the present Chapter is organized as follows: generic meteorological and PM considerations are firstly presented, followed by univariate analysis of elemental data, with enrichment factor considerations; SOM the first chemometric analysis reported, allowing the discrimination of SD events from "normal" pollution in Munich. Finally, two insights are considered: the one about SD events, with synoptic, back-trajectories and SEM-EDX analyses, and the second one about the period not affected by SD, that allowed the pollution in Munich to be evaluated by Varimax.

3.1. PM_{10}, $PM_{2.5}$ and PM_1 concentration levels

Based on the data obtained from both the OPS and meteorological station, a general description of the atmospheric conditions in Munich for the period under investigation could be drawn. Fig. 2 reports the time series of meteorological conditions. Temperature (T) and relative humidity (RH) followed, in general, the typical diurnal cycle with minima of T and maxima of RH during the night and the reverse during the day. Exceptions were detected at the beginning of SD influence over the Munich airshed. In fact, between 16th and18th March, high and almost constant values of RH were observed with T also

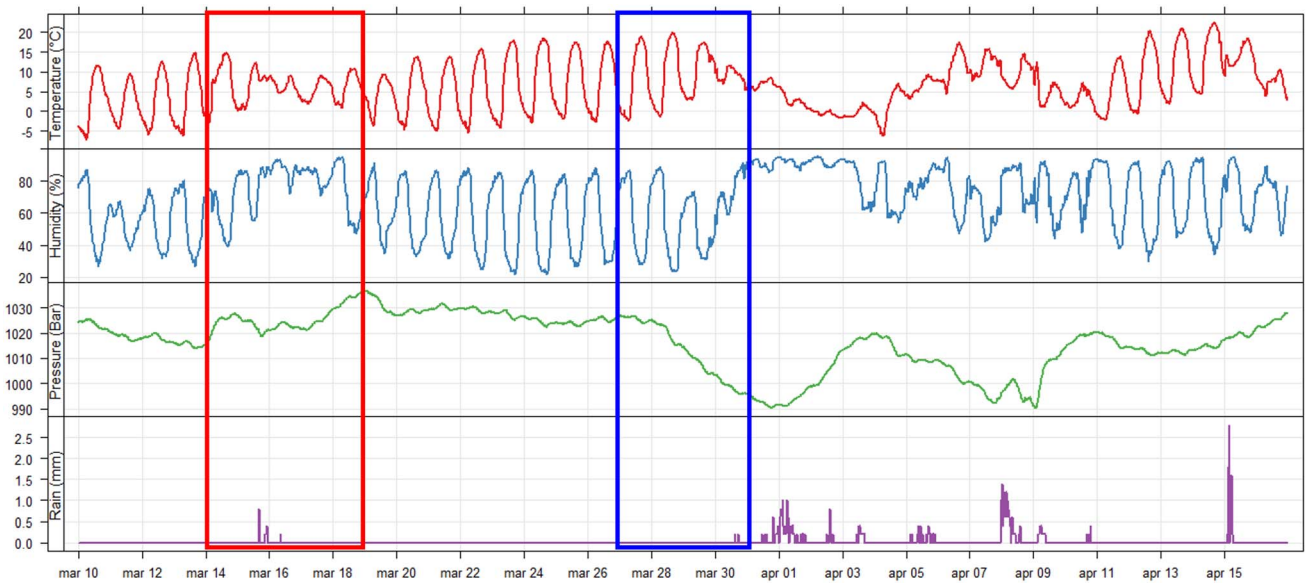

Fig. 2 Time series of atmospheric conditions in the period 10th March–15th April: temperature (°C), humidity (%), pressure (bar), and rain (mm). The red rectangle indicates the period of the first SD (14th–18th March), the blue one indicates the second SD (27th–30th March).

almost constantly oscillating around 5 °C. The same could be observed at the end of March, when, starting from 28th March, barometric pressure showed a drastic lowering, while RH increased and T decreased. Besides the concurrence of the second SD incursion into Munich, this behavior was connected with the onset of a rainy period that lasted until 10th April (see further information in the detailed meteo-climatic description accompanying the back-trajectory analysis).

Fig. 3 reports the time series of PM mass loads in the three basic cut-off metrics (PM_{10}, $PM_{2.5}$, and PM_1) together with the corresponding size distributions, respectively, covering super- and sub-micron ranges, which characterize aerosol fine and coarse fractions.

During the analyzed period, the minimum values for PM_1 and for $PM_{2.5}$ (0.52 μg m^{-3} and 1.2 μg m^{-3}, respectively) were registered on 7th April, while PM_{10} minimum (2.4 μg m^{-3}) was recorded on 8th April due to the passage of a front causing PM wet removal by precipitation (see Fig. 2). The maxima values for PM_1 and $PM_{2.5}$ of 30 μg m^{-3} and 33 μg m^{-3}, respectively, were registered on 17th March (during the first SD event), while for PM_{10} it resulted in 48.03 μg m^{-3} on 29th March (second SD event).

During the first SD event, the concentrations of PM_1, $PM_{2.5}$, and PM_{10} (Fig. 3) showed an increasing pattern followed by a limited decrease around 15th–16th March due to wet removal during the front transit and a subsequent increase reaching its maximum during the second SD event. During the last day of the second SD event, on 30th March, PM_{10} reached its maximum concentration. Subsequently, there were several rainfall events (Fig. 2) that led to a general decrease in PM concentrations.

From OPS data, huge differences in size distributions (Fig. 3b and c) and mass loads (Fig. 3a) were observed in March 2022 with high values of both parameters indicating the influence of air masses with different origins compared to those registered in April. The relevance of coarse fractions (Fig. 3c) in the investigated data reveals the influence of a source not compatible with local air pollution sources, characterized by high temperature-related sources (*i.e.* from transport, industry, and energy production) and, therefore, typically dominated by fine particles. Moreover, this effect lasted for a relatively long period, unusual in an urban airshed[55] and a relatively cold season, while the increase in the coarse PM fraction is usually detected in the summer in coincidence with increased soil aridity and consequent resuspension.[56] This occurrence, however, is in agreement with the known behavior of SD events,[57] which are characterized by considerable fractions of coarse particles.[5] This is due to the effect of weathering on lithogenic materials in arid conditions.[58] Nevertheless, SD events are accompanied by increases in finer particles associated with clay mineral components in desert dust.[59] To disclose such occurrence, a meteorological analysis was performed as described in Paragraph 3.4.

3.2. ICP-MS trace element analysis results

Descriptive statistics for the elemental composition of 24 h $PM_{2.5}$ samples determined by ICP-MS are reported in Table 1.

Based on the mean values, the most abundant elements found in the Munich airshed are Na (1747 ng m^{-3}), K (566 ng m^{-3}), and S (519 ng m^{-3}), while Zn (52.1 ng m^{-3}) is the most abundant trace element, followed by Mn (27.4 ng m^{-3}) and Cu (2.91 ng m^{-3}). The first step of data analysis consisted in enrichment factor (EF) computation. Fig. 4 reports mean and median values of the EFs, classified as a function of increasing enrichment. Elements, in fact, have an environmental fate (in this case an atmospheric fate), which reflects its emission source and, in particular, the specific processing leading to

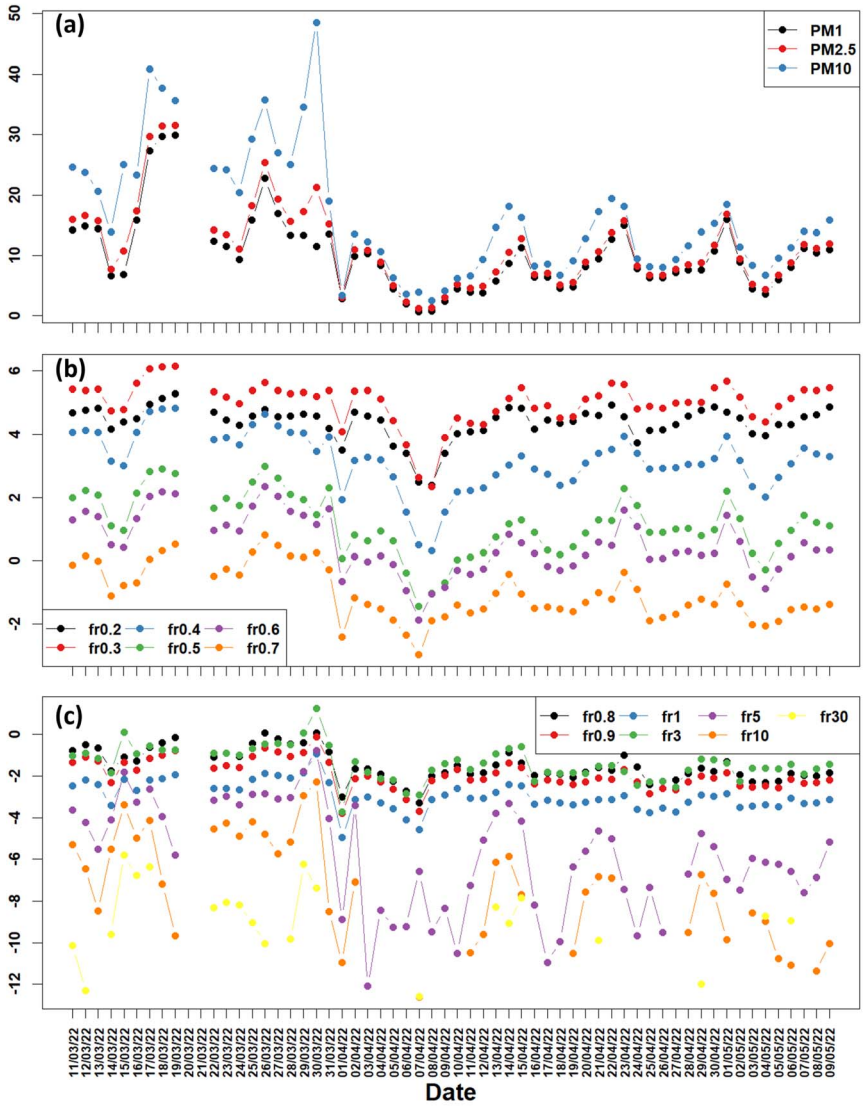

Fig. 3 Time series (daily average) from OPS data of (a) PM_1, $PM_{2.5}$, and PM_{10} (in $\mu g\ m^{-3}$), (b) fine, and (c) coarse particle fractions (in particles per cm^3, logarithmic scale). Discontinuities are due to missing data from the days 20th and 21st March. Reported size fractions correspond to: fr0.2 bin size 0.15–0.2 μm; fr0.3 0.2–0.3 μm; fr0.4 0.3–0.4 μm; fr0.5 0.4–0.5 μm; fr0.6 0.5–0.6 μm; fr0.7 0.6–0.7 μm; fr0.8 0.7–0.8 μm; fr0.9 0.8–0.9 μm; fr1 0.9–1.0 μm; fr3 1.0–3.0 μm; fr5 3.0–5.0 μm; fr10 5.0–10.0 μm; fr30 10.0 μm to the last bin, namely 26.4 μm.

a volatilization enhancement. Volatilization may be due to winds (*e.g.* dynamical/meteorologically-driven conditions, grinding/abrasion processes) and/or high-temperature processes, ranging from the natural ones (volcanoes) to the man-made ones, mostly related to the extensive use of combustion. In general, $1 \leq EF \leq 10$ is typical of not enriched elements as compared to crustal material of lithogenic origin, while $EF > 10$ is sensibly enriched. When EFs reach values of the order of 200 or more (very enriched elements), this is usually attributable to high-temperature processes promoting a fractionation of species with emphasis on the most volatile ones, which are more abundantly released, eventually condensing as/mixing with aerosol particles.

In this study, the not-enriched elements were the typical crustal ones (Ca, Mg, Sr, and Fe) together with V and Co, which may have both natural (lithogenic) and anthropogenic sources.[60,61] It is interesting to note that, despite crustal elements not showing any enrichment during the investigated period, their concentrations reached above average values in the first half of the sampling campaign with an absolute maximum on 29th March (see Paragraph 3.6 for further details). The peak on 29th March was observed also for Al, in agreement with mineral dust composition.

The second group of elements, with $10 < EF < 200$, was considered as sensibly enriched. This group included K, Na, Cr, Mn, Sb, and Ni, which may have derived from traffic and/or industrial activity.[62–66] The enrichment of Na considering the

Table 1 Basic statistics of the analyzed trace elements, in decreasing order of mean values. All values are in ng m^{-3}

	Mean	Median	Standard deviation	Minimum	Maximum
Na	1747	1773	325	706	2445
K	566	339	591	148	2907
S	519	499	278	83.4	1236
Ca	109	92.5	50.7	52.3	354
Fe	107.2	81.3	66.6	26.0	352.9
Al	56.9	39.1	56.1	16.8	315
Zn	52.1	35.8	47.8	7.87	273.5
Mg	45.5	41.3	19.4	21.4	137
Mn	27.4	4.72	47.9	0.66	190.8
Cu	2.91	2.57	1.54	0.71	6.43
Ba	2.81	2.31	1.71	0.850	8.51
Pb	2.19	1.85	1.45	0.400	7.48
Cr	1.82	1.75	0.68	0.91	4.41
Ni	1.47	1.07	1.13	0.47	8.18
Sr	0.534	0.410	0.370	0.270	2.61
Se	0.396	0.360	0.216	0.050	1.05
Mo	0.346	0.300	0.154	0.160	0.940
As	0.327	0.270	0.241	0.030	1.26
V	0.224	0.200	0.129	0.060	0.810
Sb	0.214	0.190	0.131	0.020	0.630
Cd	0.090	0.080	0.058	0.020	0.34
Co	0.056	0.040	0.040	0.020	0.24

typical marine origin of this element and the continental features of Munich can be attributed to the resuspension of technical salt used for road management during the winter season and snow days[53,67,68] that in southern Germany may last until March.

Finally, highly enriched elements with EF > 200 include Pb, As, Cu, Mo, Cd, S, Ba, Zn, and Se, suggesting high-temperature sources for all of them. In particular, S and Se (EF = 9540) appeared highly enriched in association with their similar physico-chemical properties as members of the VI group, which, together with other metals and non-metals, are known for their high volatilization rate from fossil fuel burning.[69]

3.3. Self-organizing map (SOM) modeling

Trace element concentrations were used to calculate a SOM model to enlighten SD events and solve the emissive profile of the elements in the Munich airshed. Based on the first two PCA eigenvalues (6.76 and 4.07), calculated from the starting dataset (60 observations, 22 variables), the optimal SOM dimensions were found to be 7 × 4. To train the SOM, 100 epochs were calculated with a Gaussian neighborhood function and hexagonal topology. The first SOM output, presented in Fig. 5, shows the distribution of the variables calculated from the samples assigned to each unit. Black and white units (Fig. 5), respectively, represent units in which the considered variables assume the highest and the lowest values, while the greyscale represents the quartiles of variable distributions. Therefore, based on color distribution, a visual assessment of correlations among the variables could be obtained. Indeed, Mg, Ca, and Sr showed very similar profiles due to elemental group affinity being all alkaline earths, while the association with Al and, to a lesser extent, V was attributable to the common crustal lithogenic origin. S, Se, and, to a lesser extent, Pb presented similar patterns suggesting the emission of a coal-fired power plant.[69,70] In addition, the group composed of Fe, Cu, Cd, Sb, Mo, and Ba suggested the influence of traffic.[71] The other elements (Na, K, Cr, Mn, Co, Ni, Zn, and As) did not feature similar distribution patterns suggesting multiple sources with partial sharing of specific tracers and lower individual source intensities, which, together with the low number of observed data available for the current analysis, indicated higher uncertainties in the emission profile resolutions.

SOM unit patterns were, in turn, subjected to cluster analyses to reveal SOM grouping using a more robust and consistent

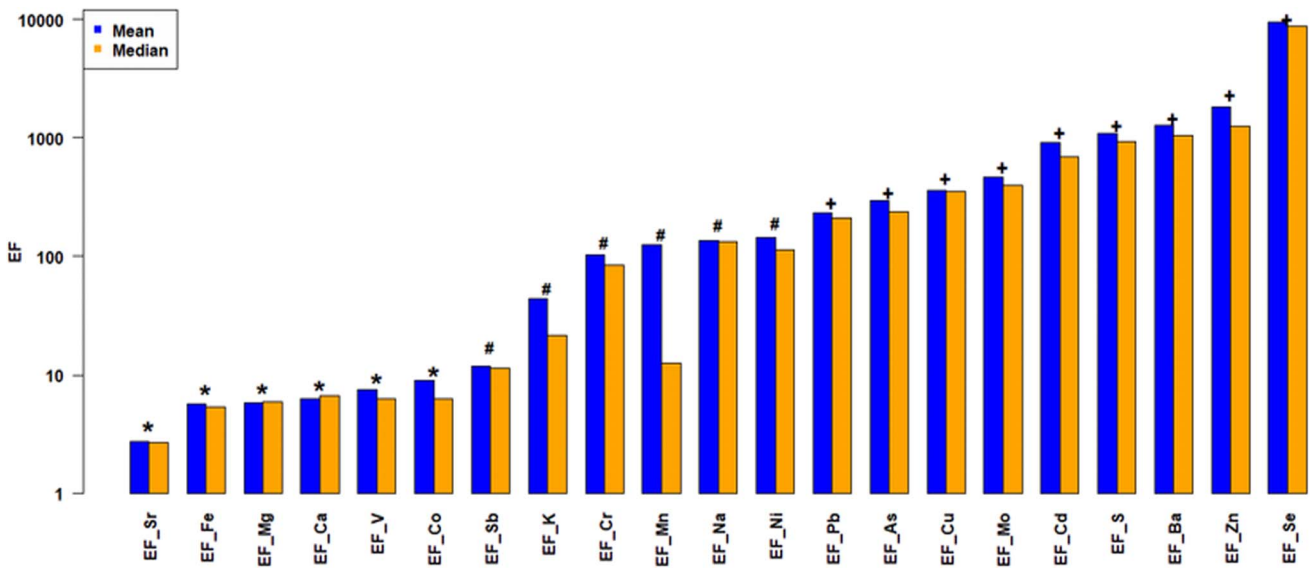

Fig. 4 Enrichment factors (EF) of the analyzed trace elements over the whole sampling period (mean: blue; median: orange). Symbols over the bars indicate not enriched (*), sensibly enriched (#), and very enriched (+) elements.

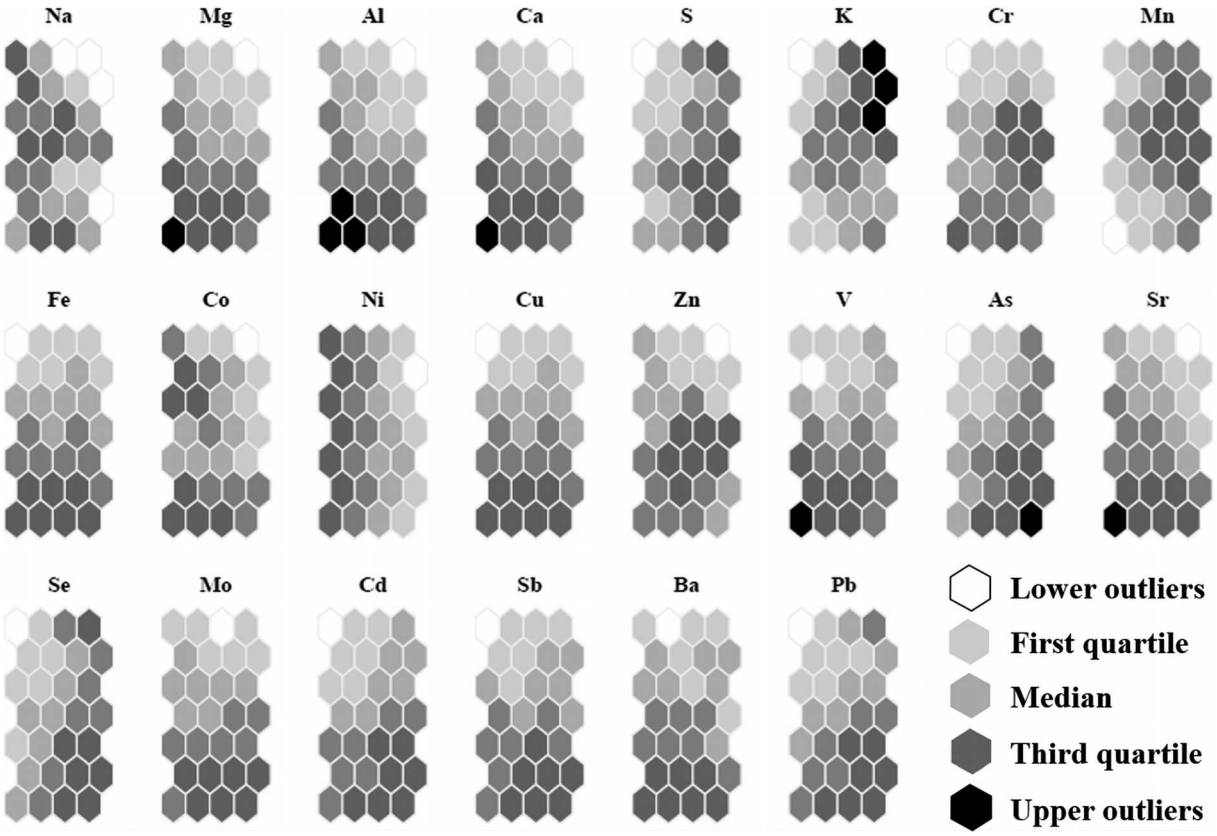

Fig. 5 Metal distribution in SOM units. From white to black, colors represent the concentrations of the single elements (as compared with the distributions of all samples) in each unit. White: lower outliers; greyscale: 1st quartile, median, 3rd quartile; black: upper outliers.

approach. In the present case, the optimized number of clusters (CL) based on minimization of the DB index[47] was five (Fig. 6). The cluster split is reported in Fig. 6a, while Fig. 6b shows the variables' behavior in each cluster. Boxplots in Fig. 6b were computed by auto-scaling each variable (*i.e.* the mean of each trace element was subtracted from each observed value and the result was normalized by its standard deviation). Typically, such normalization is used to compare variables that have different ranges of variability and, in some cases, also different units of measure.

As a result, Fig. 6 shows that the computed SOM resolved the dataset by means of two major groups: the lower region, composed of Clusters 2 (14 observations) and 3 (6 observations), represents all SD events observed; the upper region, including CL1 (14 observations), CL4 (16 observations), and CL5 (11 observations), covers local air pollution conditions in this season. CL2 and CL3 included the period 12th–30th March with all observations between 27th and 30th March (plus 12th March) assigned to CL3, and the other days (plus the days 14th–15th April and 9th May) assigned to CL2. All remaining days from March 31st to May 11th, not affected by SD, were assigned to the higher portion of the map.

Based on Wilcoxon–Mann–Whitney test, for each variable, differences between the mean values of the full dataset and that reported in SOM clusters (represented as the "zero" straight line due to auto-scaling in Fig. 6b) were considered as significant if p-values were < 0.01. As reported in Fig. 6b, all CL1-data were close to the general mean and represented the build-up of ground-level PM pollution from the local sources in dry conditions and in agreement with the sampling cut-off ($PM_{2.5}$) adopted in this work. CL4 showed significant depletions in many elements including S, which represented the non-negligible secondary sulfate component due to wet removal. CL5 was enriched in K suggesting the influence of biomass burning from the local district. In the absence of ion chromatography data, this attribution was supported mainly by the $PM_{2.5}$ cut-off as well as by the relatively mild mineralization conditions prior to ICP-MS analysis: these allowed the quantitative recovery of soluble K^+ but were insufficient in the case of a mineral matrix. A mineral K contribution, in fact, would have populated the coarse fraction, herein excluded.[72,73]

The lower map region, in turn, could be used to describe SD events. A preliminary analysis of the SD events based on remote sensing data revealed that the plume remained trapped over the region for several days mixing with local aerosol sources (aged aerosol conditions) before being removed. Such considerations were confirmed by the temporal trend of PM registered by the OPS.

Cluster 2 was characterized by significantly higher concentration levels of Fe, Cu, As, Se, Mo, Cd, Sb, Ba, Pb, and partially S and Ca (p-values = 0.00278 and 0.00149, respectively). These elements are mostly markers of anthropogenic sources.[74,75]

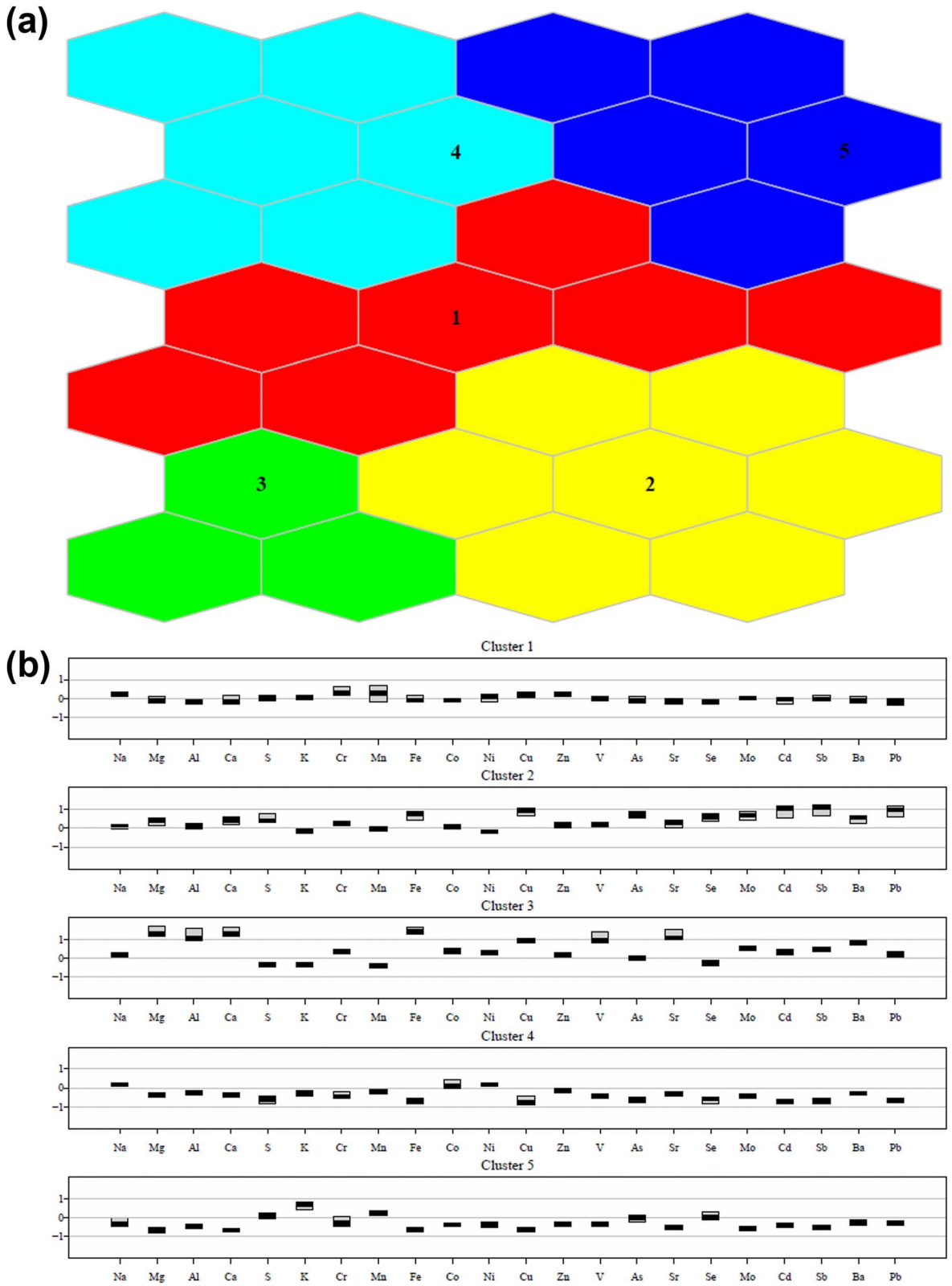

Fig. 6 (a) SOM map divided by clusters by the k-means algorithm and DB index. Cluster numbers are placed in the centroid units; (b) boxplots of elements based on SOM cluster division. Data are auto-scaled based on the mean and standard deviation of the whole dataset.

Their increase in the SD period could be reconstructed by means of the transport pattern of the air mass (as described in detail in the following paragraph 3.4) before reaching Munich. This slower transport phase suggests an enrichment mechanism during the transport over continental Europe and the permanence of the air mass over the Munich airshed producing

"aged aerosol" with mixed characteristics. Cluster 3, instead, included the period of the second SD event and was characterized by extremely high concentration increases of crustal elements: Mg, Al, Ca, Fe, and Sr, besides Cu and V. These elements were the most representative of an LRT-SD event,[76] in agreement with the straight transportation path followed by this dust and with OPS size distribution data for the involved period.

3.4. Synoptic analysis of saharan dust events

As anticipated above, to substantiate the results of PM chemical speciation and source apportionment, a detailed synoptic meteorological analysis was conducted. The first, most intense LRT-SD event of 14th–18th March 2022 impacted severely many regions in Western Europe (*e.g.* Portugal, Spain, and France), as documented in several news and social media and some scientific papers.[2,7]

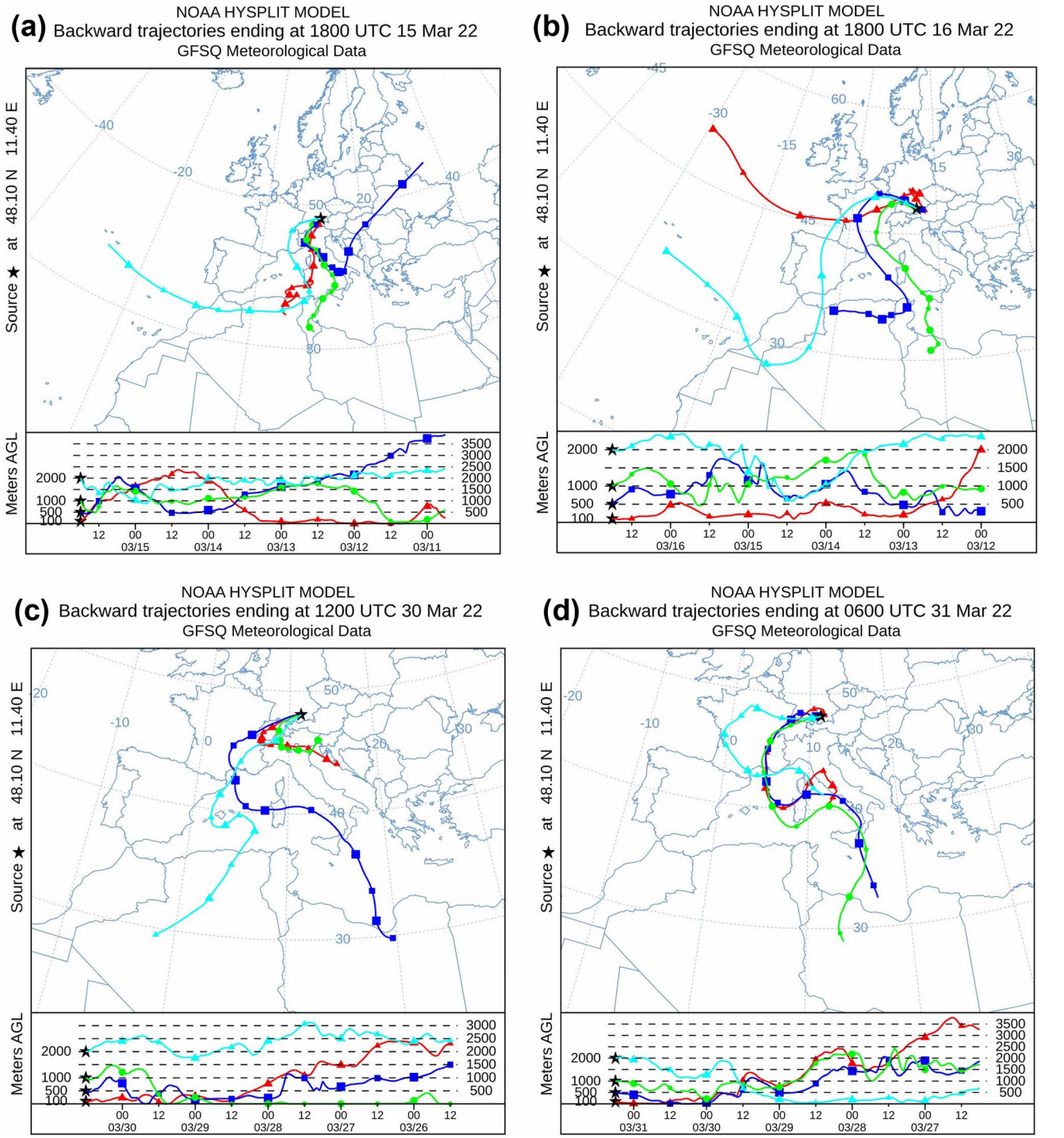

Fig. 7 Back trajectories (120 h backward) for the two SD events (upper part: first event; lower part: second event) ending at Munich on (a) 15th March at 18:00 UTC (first SD), (b) 16th March at 18:00 UTC, (c) 30th March at 12:00 UTC, and (d) 31st March at 6:00 UTC.

The event originated in northwestern Africa, specifically in Morocco/Algeria, and was associated with a peculiar type of storm, named Dust-Infused Baroclinic Storm (DIBS),[77] characterized by icy clouds permeated with dust. Indeed, owing to the strong ascending motions characterizing the DIBS, they have been associated with dusty cirrus decks formed or at least affected by the transport of mineral dust to the upper troposphere.[78] Specifically, in mid-March 2022, an atmospheric river of desert dust was entrained by a DIBS uplifting dust particles at upper tropospheric levels up to 10 km.[79] There, dust favored the nucleation of ice particles leading to the formation of an extended icy dust-infused cirrus cloud deck.[79] According to reports from Copernicus (CAMS2_71 PM10 episode 13th–18th March 2022 v1),[80] NASA Earth Observatory[81] and Seifert *et al.* (2023),[79] the so-formed dusty air mass was spread over large part of Europe and also Asia persisting for nearly one week. The atmospheric river (or warm conveyor belt) and intense dust uplift was associated with the storm Celia and further facilitated by the combination of a low-pressure system south-west of the Iberian Peninsula and a high-pressure area over Central/Northern Europe.

Synoptic maps for 14th–17th March (Fig. S1†) show the presence of a low-pressure system over north-western Africa (storm Celia originated on 13th March). The stormy and rainy weather spread from south to north over 13th–14th March entraining dust from the Sahara Desert. As evidenced by the synoptic maps and the multi-model dust optical depth retrieved from the WMO Barcelona Dust Regional Center[82] (Fig. S2†), the atmospheric dust river was first propagated to Portugal, Spain, and France (explaining the peculiar trace elements profile observed in SOM analysis) and then reached western and central Europe in the following days. A detailed analysis showed that during this event, the dust river led to the formation of two separate DIBS, of which the second one most probably was transported to Munich. The first storm started on 15th March 2022 over north-central Europe and spread from Poland, Czech Republic, and Austria south to the eastern Mediterranean. The second storm started on 16th March and was directly connected

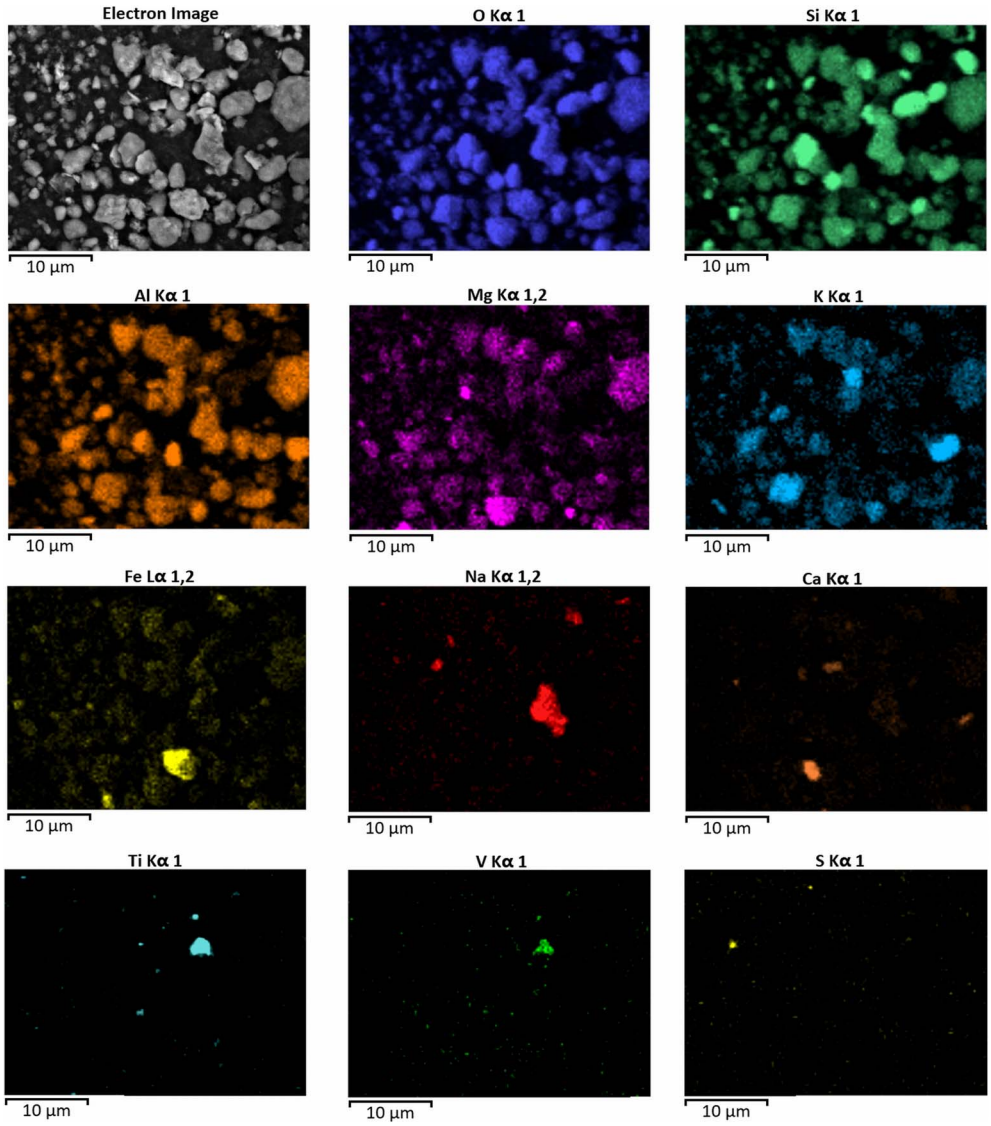

Fig. 8 Elemental distribution of particles from the SD event by SEM/EDX at 12 kV.

to the desert dust source moving north over Europe and then east over Russia. Back-trajectory analyses of 15th and 16th March are reported in Fig. 7a and b. Fig. S3† shows the vertical profiles of attenuated backscatter coefficients for those days. The attenuated backscatter coefficient is an atmospheric parameter which determines the strength of the lidar signal and describes how much light is scattered in the backward direction. The image clearly shows the presence of the thick aerosol cloud at 3–4 km. The second, minor event was instead characterized by a typical southwestern transport of dust lifted from North Africa to the Mediterranean, then traveling further north over the Alps towards central Europe on 30th–31st March (Fig. 7c and d). The dust transit was associated with a northerly trough and the persistent blocking high to its south. A lower geopotential height was observed to the west, while southern and eastern Europe were characterized by high pressures (Fig. S4 and S5†). Fig. S6† shows the vertical profiles of attenuated backscatter coefficients for 30th–31st March. The figure thus shows clearly the dust cloud travelling at relatively low height levels, as evidenced by the high signal recorded especially on 30th March.

3.5. SEM-EDX analysis

In order to further describe the SD events, Fig. 8 shows an SEM micrograph with EDX mappings of SD particles. SEM micrographs and EDX measurements provided significant additional information regarding the particles' distribution and chemical composition during the SD events.

As can be noted from Fig. 8, SD particles showed relevant contributions from aluminosilicates and magnesium aluminosilicates with lower amounts of quartz crystals. Silicates were present mainly in the form of kaolinite and smectite, as usually reported for SD aerosols (*e.g.* ref. 57). Additionally, K-enriched particles were detected, which were assigned to illite and Mg-enriched members of the illite-aluminoceladonite series as well as Na-enriched particles matching the chemical profile of oligoclase or other members of the closely related plagioclase feldspar series.[83] Ca-enriched particles were detected in SD samples, which could be attributed to calcite ($CaCO_3$) and lime (CaO). Furthermore, particles of iron oxide, most likely hematite, responsible for the reddish color of mineral dust[84] and TiO_2 with V encrustations were observed. S-enriched particles were only observed in the submicron size range, which literature associates with secondary ammonium sulphate although it also possibly originates from gypsum.[85]

These results support the hypothesis of SD influence over the Munich airshed, based on the above mineralogical observation, and are in overall agreement with the evidence obtained by elemental analysis and meteoclimatic assessment previously discussed.

3.6. Varimax analysis for the description of Munich pollution

Varimax analysis was applied to both the entire dataset and the days between March 31st and May 11th only. The aim was to find correlations between the element concentrations in the entire study period and in the period not affected by SD in order to describe the main air pollution sources in Munich. Table 2 reports Varimax loadings for the model computed with the entire dataset, while Varimax loadings for the reduced dataset are reported in Table S1.† In both cases, the best results were obtained with six factors explaining 79.2% of the total variance for the full dataset and 77.0% for the reduced one. The comparison between Tables 2 and S2† indicates very similar results considering the variables associated in each factor, although the factors may be different. Therefore, the conclusions drawn for the full dataset were similar to those obtained by removing the presence of SD events from the dataset.

Each Varimax factor could be assigned to a specific air pollution source based on a comparison with the literature and datasets containing consolidated source chemical profiles and their fingerprints (*e.g.* SPECIEUROPE) as shared within the international scientific community.[86] The obtained results agree with the observations reported in EF and SOM discussions, with Varimax factors correlating groups of elements similarly to what was previously observed. The advantage of Varimax is that it can be used to strengthen the evaluation of correlation between variables that with SOM can be deduced only (or mainly) visually.

Therefore, Factor 1 (23.9% EV corresponding to Factor 2 in Table S2†) was dominated by elements of crustal origin including Mg, Al, Ca, Fe, V, and Sr, typically considered to be associated with soil and road resuspension and possibly including local and long-range sources. This source usually prevails in the coarse mode of PM sensibly contributing to its mass load. It is interesting to observe that the chemical

Table 2 Varimax loadings for elemental concentrations in the full-dataset case. Bold values correspond to the most representative variables for each factor, EV stands for the explained variance

	Factor 1	Factor 2	Factor 3	Factor 4	Factor 5	Factor 6
EV (%)	23.9	20.4	13.4	9.0	6.6	5.9
Na	−0.052	−0.415	**0.533**	0.085	−0.070	−0.208
Mg	**0.886**	−0.003	0.314	−0.012	0.150	0.038
Al	**0.896**	0.007	−0.002	−0.003	0.149	−0.041
Ca	**0.904**	0.059	0.247	−0.125	0.164	0.053
S	−0.082	**0.879**	−0.198	0.149	0.055	0.045
K	−0.099	0.077	−0.134	0.223	**−0.814**	−0.163
Cr	0.119	0.035	0.326	**0.873**	0.056	0.099
Mn	−0.166	−0.007	0.003	**0.915**	−0.180	0.044
Fe	**0.760**	0.210	0.495	0.130	0.013	0.078
Co	0.458	−0.044	−0.049	0.021	−0.108	0.473
Ni	0.349	−0.089	−0.275	0.060	0.609	−0.140
Cu	0.251	0.328	**0.753**	0.143	0.015	0.018
Zn	0.116	−0.022	0.042	−0.096	−0.081	**−0.857**
V	**0.859**	0.087	−0.111	0.062	−0.099	−0.329
As	0.122	**0.798**	0.038	−0.092	−0.153	−0.269
Sr	**0.911**	0.068	0.103	−0.085	0.023	0.094
Se	−0.073	**0.901**	−0.018	0.109	−0.136	0.044
Mo	0.136	0.190	**0.692**	0.353	0.015	−0.086
Cd	0.158	**0.836**	0.411	−0.091	0.018	0.016
Sb	0.206	**0.652**	**0.599**	−0.019	−0.018	0.112
Ba	0.358	−0.040	**0.568**	−0.246	−0.476	0.082
Pb	0.091	**0.864**	0.320	−0.009	0.035	0.044

speciation seemed to be well conserved despite the sampling cut-off of 2.5 μm employed in this work, which is supposed to prevent the collection of a large fraction of coarse particles.

The time series reported in Fig. 9a revealed that the concentrations (in ng m^{-3}) of the lithogenic elements were apparently higher during the period affected by the SD

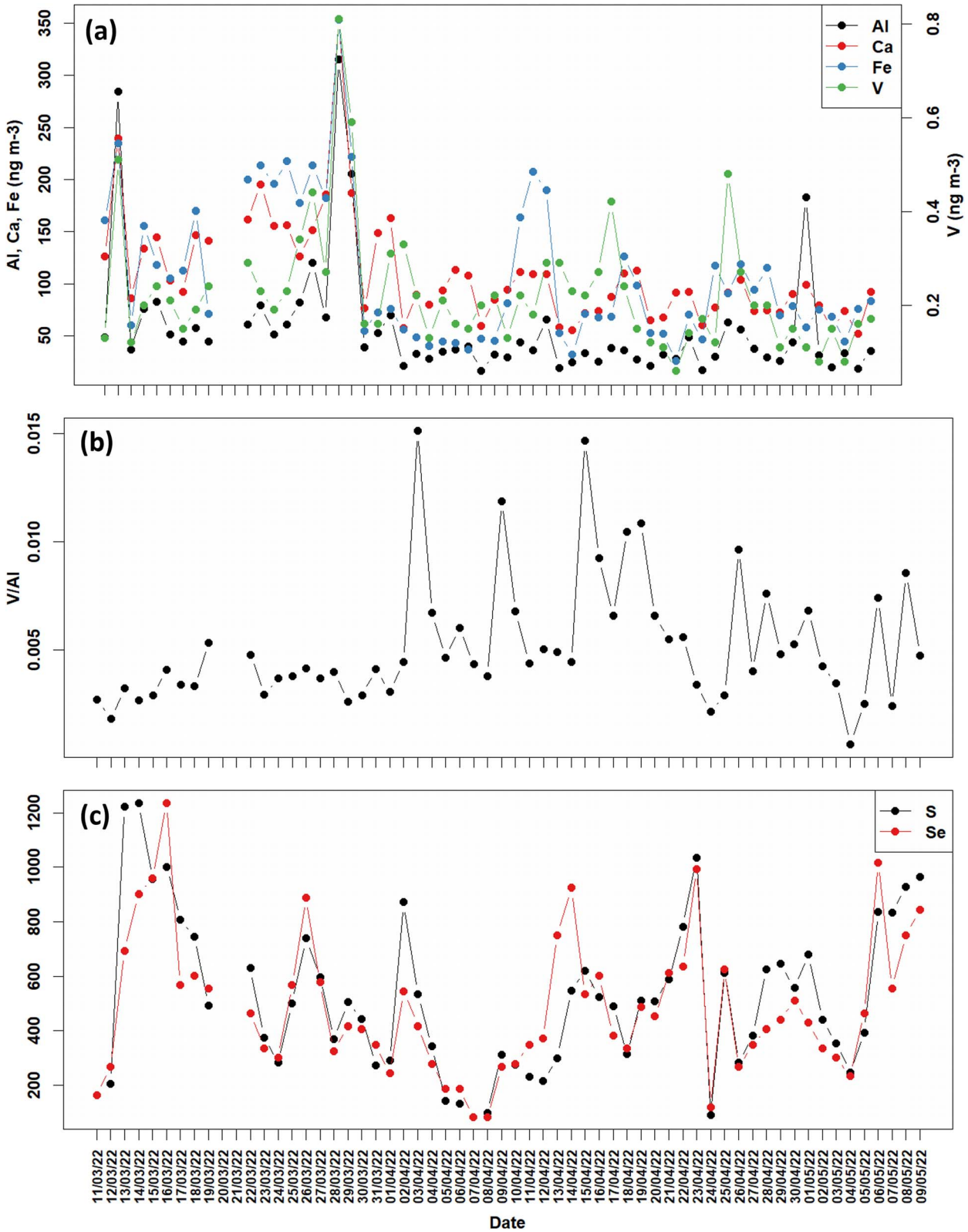

Fig. 9 Time series for (a) crustal elements (Al, Ca, Fe, and V), (b) V/Al ratio, and (c) S and Se (indicative of a coal-fired power plant). (a and b) Show visual differences between SD-affected and unaffected periods.

sequence. In fact, mean values before and after the events were, respectively, 98.4 and 39.5 for Al, 160 and 88.0 for Ca, 178 and 78.5 for Fe and 0.299 and 0.192 for V. The ratios between SD-affected and not-SD-affected days for these elements ranged from 1.5 (for V) to 2.5 (for Al). For comparison, Öztürk and Keleş (2016)[87] had found ratios between 1.3 (for V) to more than 3 (for crustal elements such as Al). Such huge differences between the SD-affected and SD-unaffected periods were even better enlightened by the time series of the V/Al ratio, reported in Fig. 9b. SD-affected days showed a value close to $1.8–5.3\times10^{-3}$, as reported for soil and SD material, while from April onward, the ratio assumed values up to one order of magnitude larger indicating the influence of other sources including fossil fuel from traffic (diesel), coal burning, and possibly a steelwork plant.[88]

Factor 2 (20.5% EV corresponding to Factor 1 in Table S1†) included S, As, Se, Cd, Sb, and Pb. These elements reflect the influence of emissions from a coal-fired power plant in agreement with previous works.[69] The influence of this source, typically dominating the submicron fraction, was detected throughout the measurement period, in agreement with its localization. Though coal is not the only source of S (see the intercept different from zero in Fig. S7†) it appeared highly correlated with Se, in agreement with other studies suggesting a diagnostic ratio for coal ranging between 1000 and 3400 with the higher values typical of increasing age of air masses.[89] The ratio S/Se (Fig. S8†) oscillated around an average value of 1355 (median 1364) throughout the period, while the time trends of both these elements were very similar (Fig. 9c) with a Spearman's correlation index of 0.83 (Fig. S8†).

It should be noted how EF for S peaked in correspondence with the major SD events, in agreement with the presence of gypsum, while in the second part of the campaign described in this work, there was a tendency towards higher enrichment in S in $PM_{2.5}$, where it is typically found in the form of secondary sulfate.[73] Such an increase was observed in coincidence with the enhanced photochemistry in the milder season, efficiently activating SO_2 conversion into sulfate.[90]

Factor 3 (13.4% EV) included Na and Cu, Mo, Sb, and Ba. Therefore, it could be considered as non-exhaust traffic source, which is mainly characterized by mechanically generated particles *i.e.* abrasion and friction with dominating elements such as Cu, Sb, and Ba from brakes and Mo from metal components.[71] The occurrence of Na, instead, could be attributed to winter road management and the use of road technical salt, mainly composed of NaCl.[53,67,68]

Factor 4 (9.0% EV) showed a relevant contribution of Cr and Mn suggesting the influence of a high-temperature emission.[91] The absence of correlation of these two elements with Al and Ca excludes the possibility of a soil resuspension source. A possible source for these elements could be a steelwork plant, which is present in the vicinity of Munich[92]

Factor 5 (6.6% EV) included only K as a statistically significant factor constituent. The absence of correlation with other inorganic tracers, as in the case of CL5 for the SOM, suggests that this element was likely associated with biomass burning, wherein it is characterized by its ionic form, most likely from domestic heating by woodstoves or similar devices, as confirmed by the aerosol cutoff employed. Indeed, a mineral source for K would require a coarse fraction, not included in this sampling cutoff, and correlation with other geogenic elements.

Finally, Factor 6 (5.9% EV) was characterized by Zn only suggesting a waste incinerator plant as the contributing emission source.[93] The fine fraction always reveals high temperature source emissions and Zn is a typical waste incinerator tracer. Such waste management plants are present in Munich, north of the sampling point.[94]

4. Conclusions

Two Saharan dust events were observed in the Munich (Germany) airshed in March 2022. Comprehensive analysis of elemental profiles by ICP-MS and SEM-EDX, metrodynamics, and remote sensing by optical particle spectrometry allowed a full analysis of both Saharan dust events and a preliminary particulate matter source apportionment to be performed based on inorganic species for the city of Munich.

The dust events were identified and characterized by back-trajectory and self-organizing map analyses. Back trajectories revealed, associated with the presence of a Dust-Infused Baroclinic Storm, for the first event a transport pathway across Spain and France before reaching Germany, while the second event reflected a frequently observed transportation pattern except for its long-range transport. Finally, SOM allowed the days of major impact from dust events in Munich to be unravelled based on Fe, Cu, As, Se, Mo, Cd, Sb, Ba, and Pb for the first event (associated with the presence of aged aerosol) and Mg, Al, Ca, Fe, and Sr (crustal elements) for the second one. SEM-EDX analysis confirmed the presence of Saharan dust events in the airsheds above Munich, characterized by significant concentrations of aluminosilicates and magnesium aluminosilicates.

The source apportionment by Varimax, together with enrichment factors, showed that the Munich airshed is affected by a range of well-defined local anthropogenic emission sources, such as traffic, energy production by coal combustion, industry, and waste incineration.

Data availability

The data supporting this article have been included as part of the manuscript as well as the ESI.†

Conflicts of interest

The authors declare that they have no conflict of interest.

Acknowledgements

This research is funded by dtec.bw – Digitalization and Technology Research Center of the Bundeswehr [project MORE]. Dtec.bw is funded by the European Union – NextGenerationEU. We acknowledge financial support by Universität der Bundeswehr München. This paper is published with the contribution

of the Department of Excellence program financed by the Ministry of Education, University and Research (MIUR, L. 232 del 01/12/2016). The HYSPLIT transport and dispersion model and/or READY website (https://www.ready.noaa.gov) used in this publication were provided by the NOAA Air Resources Laboratory (ARL). We thank the Zentralanstalt für Meteorologie und Geodynamik (ZAMG), Austria, for the synoptic analysis' images. We also thank the Alice-net automated LIDAR ceilometer network for providing access to the LIDAR ceilometer images from Oberschleissheim (Munich, Germany).

References

1 A. Adebiyi, J. F. Kok, B. J. Murray, C. L. Ryder, J.-B. W. Stuut, R. A. Kahn, P. Knippertz, P. Formenti, N. M. Mahowald, C. Pérez García-Pando, M. Klose, A. Ansmann, B. H. Samset, A. Ito, Y. Balkanski, C. Di Biagio, M. N. Romanias, Y. Huang and J. Meng, *Aeolian Res.*, 2023, **60**, 100849.
2 D. Francis, R. Fonseca, N. Nelli, D. Bozkurt, G. Picard and B. Guan, *Atmos. Res.*, 2022, **266**, 105959.
3 R. G. Harrison, K. A. Nicoll, G. J. Marlton, C. L. Ryder and A. J. Bennett, *Environ. Res. Lett.*, 2018, **13**, 054018.
4 D. M. Szczepanik, I. S. Stachlewska, E. Tetoni and D. Althausen, *Earth Space Sci.*, 2021, **8**, e2021EA001816.
5 L. Tositti, E. Brattich, C. Cassardo, P. Morozzi, A. Bracci, A. Marinoni, S. Di Sabatino, F. Porcù and A. Zappi, *Atmos. Chem. Phys.*, 2022, **22**, 4047–4073.
6 G. Varga, *Environ. Int.*, 2020, **139**, 105712.
7 J. Gomes, H. Esteves and L. Rente, *Gases*, 2022, **2**, 74–84.
8 A. M. Sánchez de la Campa, J. D. de la Rosa, Y. González-Castanedo, R. Fernández-Camacho, A. Alastuey, X. Querol and C. Pio, *Atmos. Res.*, 2010, **96**, 633–644.
9 T. Caton Harrison, R. Washington and S. Engelstaedter, *J. Geophys. Res.: Atmos.*, 2019, **124**, 9665–9690.
10 P. S. M. Santos, E. B. H. Santos and A. C. Duarte, *Environ. Sci. Pollut. Res.*, 2013, **20**, 227–237.
11 P. Israelevich, E. Ganor, P. Alpert, P. Kishcha and A. Stupp, *J. Geophys. Res.: Atmos.*, 2012, **117**(D2), DOI: 10.1029/2011JD016482.
12 P. Salvador, J. Pey, N. Pérez, X. Querol and B. Artíñano, *npj Clim. Atmos. Sci.*, 2022, **5**, 1–10.
13 M. Liaskoni, P. Huszar, L. Bartík, A. P. Prieto Perez, J. Karlický and O. Vlček, *Atmos. Chem. Phys.*, 2023, **23**, 3629–3654.
14 P. Morozzi, L. Bolelli, E. Brattich, E. N. Ferri, S. Girotti, S. Sangiorgi, J. A. G. Orza, F. Piñero-García and L. Tositti, *Sci. Total Environ.*, 2021, **789**, 148005.
15 E. Brattich, J. A. G. Orza, P. Cristofanelli, P. Bonasoni, A. Marinoni and L. Tositti, *Atmos. Environ.*, 2020, **234**, 117513.
16 E. Brattich, M. A. Hernández-Ceballos, G. Cinelli and L. Tositti, *Atmos. Environ.*, 2015, **112**, 136–147.
17 L. Tositti, A. Riccio, S. Sandrini, E. Brattich, D. Baldacci, S. Parmeggiani, P. Cristofanelli and P. Bonasoni, *Atmos. Environ.*, 2013, **65**, 142–152.
18 G. Varga, Á. Rostási, A. Csávics and P. Dagsson-waldhauserova, in *25th EGU General Assembly*, 2023.
19 K. R. Clifford, *Ann. Assoc. Am. Geogr.*, 2022, **112**, 2287–2304.
20 M. O. Andreae and D. Rosenfeld, *Earth-Sci. Rev.*, 2008, **89**, 13–41.
21 European Parliament, *Directive 2008/50/EC of the European Parliament and of the Council of 21 May 2008 on Ambient Air Quality and Cleaner Air for Europe*, European Commission, Brussels, Belgium, 2008.
22 M. Gini, M. Manousakas, A. G. Karydas and K. Eleftheriadis, *Environ. Pollut.*, 2022, **298**, 118768.
23 M. Kotsyfakis, S. G. Zarogiannis and E. Patelarou, *Int. J. Occup. Med. Environ. Health*, 2019, **32**, 749–760.
24 S. Z. Sajani, R. Miglio, P. Bonasoni, P. Cristofanelli, A. Marinoni, C. Sartini, C. A. Goldoni, G. De Girolamo and P. Lauriola, *Occup. Environ. Med.*, 2011, **68**, 446–451.
25 S. Sakhamuri and S. Cummings, *Lancet Planet. Health*, 2019, **3**, e242–e243.
26 Q. Wang, J. Gu and X. Wang, *Atmos. Environ.*, 2020, **241**, 117771.
27 P. Salvador, F. Molero, A. J. Fernandez, A. Tobías, M. Pandolfi, F. J. Gómez-Moreno, M. Barreiro, N. Pérez, I. M. Marco, M. A. Revuelta, X. Querol and B. Artíñano, *Atmos. Res.*, 2019, **226**, 208–218.
28 D. Rieger, A. Steiner, V. Bachmann, P. Gasch, J. Förstner, K. Deetz, B. Vogel and H. Vogel, *Atmos. Chem. Phys.*, 2017, **17**, 13391–13415.
29 H. Flentje, B. Briel, C. Beck, M. Collaud Coen, M. Fricke, J. Cyrys, J. Gu, M. Pitz and W. Thomas, *Atmos. Environ.*, 2015, **109**, 87–96.
30 Copernicus, "Historic" Saharan dust episode in western Europe – CAMS predictions accurate, https://atmosphere.copernicus.eu/historical-saharan-dust-episode-western-europe-cams-predictions-accurate, accessed July 17, 2024.
31 T. Kohonen, *Neurocomputing*, 1998, **21**, 1–6.
32 S. Licen, A. Astel and S. Tsakovski, *Sci. Total Environ.*, 2023, **878**, 163084.
33 P. Paatero and U. Tapper, *Environmetrics*, 1994, **5**, 111–126.
34 QGIS, QGIS main page, https://qgis.org/en/site/, accessed July 17, 2024.
35 X. Cao, J. Lintelmann, S. Padoan, S. Bauer, A. Huber, A. Mudan, S. Oeder, T. Adam, S. Di Bucchianico and R. Zimmermann, *Anal. Biochem.*, 2021, **618**, 114127.
36 PALAS, Fidas 200 S Air Quality Monitor, https://www.palas.de/en/product/fidas200s, accessed May 22, 2023.
37 E. Tipping, C. Woof and K. Clarke, *Hydrol. Processes*, 1993, **7**, 263–277.
38 D. C. Carslaw and K. Ropkins, *Environ. Model. Softw.*, 2012, **27–28**, 52–61.
39 D. R. Lawson and J. W. Winchester, *Atmos. Environ.*, 1979, **13**, 925–930.
40 H. Wedepohl, *Geochim. Cosmochim. Acta*, 1995, **59**, 1217–1232.
41 R. U. Shelley, P. L. Morton and W. M. Landing, *Deep Sea Res., Part II*, 2015, **116**, 262–272.

42 M. D. Gelado-Caballero, P. López-García, S. Prieto, M. D. Patey, C. Collado, J. J. Hérnández-Brito, P. López-García, S. Prieto, M. D. Patey, C. Collado and J. J. Hérnández-Brito, *J. Geophys. Res.: Atmos.*, 2012, **117**, 3304.
43 J. M. Prospero, *Chemistry of Marine Water and Sediments*, ed. A. Gianguzza, E. Pelizzetti and S. Sammartano, Springer Berlin Heidelberg, Berlin, Heidelberg, 2002, pp. 35–82.
44 R. G. Brereton, *Chem. Cent. J.*, 2012, **6**(2), S1.
45 R. Bro and A. K. Smilde, *Anal. Methods*, 2014, **6**, 2812–2831.
46 K. Nakagawa, Z. Q. Yu, R. Berndtsson and T. Hosono, *J. Hydrol.*, 2020, **582**, 124519.
47 D. L. Davies and D. W. Bouldin, *IEEE Trans. Pattern Anal. Mach. Intell.*, 1979, **PAMI-1**, 224–227.
48 S. Licen, M. Franzon, T. Rodani and P. Barbieri, *Microchem. J.*, 2021, **165**, 106181.
49 A. F. Stein, R. R. Draxler, G. D. Rolph, B. J. B. Stunder, M. D. Cohen and F. Ngan, *Bull. Am. Meteorol. Soc.*, 2015, **96**, 2059–2077.
50 G. Rolph, A. Stein and B. Stunder, *Environ. Model. Softw.*, 2017, **95**, 210–228.
51 *National Centers for Environmental Prediction/National Weather Service/NOAA/US Department of Commerce*, 2015.
52 P. Van Espen and F. Adams, *Anal. Chim. Acta*, 1983, **150**, 153–161.
53 A. Zappi, O. Popovicheva, L. Tositti, M. Chichaeva, I. Eremina, A. Kasper-Giebl, Y. I. Tsai, D. Vlasov and N. Kasimov, *Atmos. Environ.*, 2023, **294**, 119458.
54 R. Leardi, C. Melzi and G. Polotti, CAT (Chemometric Agile Tool), **http://gruppochemiometria.it/index.php/software**, accessed December 12, 2021.
55 T. Wu and B. E. Boor, *Atmos. Chem. Phys.*, 2021, **21**, 8883–8914.
56 T. V. Vu, J. M. Delgado-Saborit and R. M. Harrison, *Atmos. Environ.*, 2015, **122**, 114–132.
57 N. Mahowald, S. Albani, J. F. Kok, S. Engelstaeder, R. Scanza, D. S. Ward and M. G. Flanner, *Aeolian Res.*, 2014, **15**, 53–71.
58 F. Raes, R. Van Dingenen, E. Vignati, J. Wilson, J.-P. Putaud, J. H. Seinfeld and P. Adams, *Atmos. Environ.*, 2000, **34**, 4215–4240.
59 N. Mahowald, T. D. Jickells, A. R. Baker, P. Artaxo, C. R. Benitez-Nelson, G. Bergametti, T. C. Bond, Y. Chen, D. D. Cohen, B. Herut, N. Kubilay, R. Losno, C. Luo, W. Maenhaut, K. A. McGee, G. S. Okin, R. L. Siefert and S. Tsukuda, *Global Biogeochem. Cycles*, 2008, **22**(4), DOI: **10.1029/2008GB003240**.
60 X. Bai, L. Luo, H. Tian, S. Liu, Y. Hao, S. Zhao, S. Lin, C. Zhu, Z. Guo and Y. Lv, *Environ. Sci. Technol.*, 2021, **55**, 11568–11578.
61 A. Penezić, A. Milinković, S. Bakija Alempijević, S. Žužul and S. Frka, *Chemosphere*, 2021, **283**, 131178.
62 S. M. Almeida, M. C. Freitas, M. A. Reis, C. A. Pio and M. A. Trancoso, *Nucl. Instrum. Methods Phys. Res. A.*, 2006, **564**, 752–760.
63 J. C. Chow, D. H. Lowental, L. W. A. Chen, X. Wang and J. G. Watson, *Air Qual., Atmos. Health*, 2015, **8**, 243–263.
64 J. E. Pachon, R. J. Weber, X. Zhang, J. A. Mulholland and A. G. Russell, *Atmos. Pollut. Res.*, 2013, **4**, 14–21.
65 G. Palladino, P. Morozzi, E. Biagi, E. Brattich, S. Turroni, S. Rampelli, L. Tositti and M. Candela, *Sci. Rep.*, 2021, **11**, 1–12.
66 J. S. Reid, R. Koppmann, T. F. Eck and D. P. Eleuterio, *Atmos. Chem. Phys.*, 2005, **5**, 799–825.
67 L. Tositti, E. Brattich, M. Masiol, D. Baldacci, D. Ceccato, S. Parmeggiani, M. Stracquadanio and S. Zappoli, *Environ. Sci. Pollut. Res.*, 2014, **21**, 872–890.
68 S. M. McNamara, K. R. Kolesar, S. Wang, R. M. Kirpes, N. W. May, M. J. Gunsch, R. D. Cook, J. D. Fuentes, R. S. Hornbrook, E. C. Apel, S. China, A. Laskin and K. A. Pratt, *ACS Cent. Sci.*, 2020, **6**, 684–694.
69 H. Nalbandian, IEA Clean Coal Center, **https://usea.org/sites/default/files/092012_Trace/element/emissions/fromcoal_ccc203.pdf**, 2012.
70 J. G. Watson, J. C. Chow, D. H. Lowenthal, N. F. Robinson, C. F. Cahill and D. L. Blumenthal, *Energy Fuels*, 2002, **16**, 311–324.
71 A. Thorpe and R. M. Harrison, *Sci. Total Environ.*, 2008, **400**, 270–282.
72 F. Cao, S.-C. Zhang, K. Kawamura and Y.-L. Zhang, *Sci. Total Environ.*, 2016, **572**, 1244–1251.
73 L. Tositti, P. Morozzi, E. Brattich, A. Zappi, M. Calvello, F. Esposito, A. Lettino, G. Pavese, S. Sabia, A. Speranza, V. Summa and R. Caggiano, *Sci. Total Environ.*, 2022, **851**, 158127.
74 L. Han, G. Zhuang, S. Cheng and J. Li, *Atmos. Environ.*, 2007, **41**, 7533–7546.
75 C. Madsen, K. C. L. Carlsen, G. Hoek, B. Oftedal, P. Nafstad, K. Meliefste, R. Jacobsen, W. Nystad, K.-H. Carlsen and B. Brunekreef, *Atmos. Environ.*, 2007, **41**, 7500–7511.
76 P. Formenti, S. Caquineau, K. Desboeufs, A. Klaver, S. Chevaillier, E. Journet and J. L. Rajot, *Atmos. Chem. Phys.*, 2014, **14**, 10663–10686.
77 M. Fromm, G. Kablick and P. Caffrey, *Geophys. Res. Lett.*, 2016, **43**(12), 643–650.
78 A. Ansmann, R.-E. Mamouri, J. Bühl, P. Seifert, R. Engelmann, J. Hofer, A. Nisantzi, J. D. Atkinson, Z. A. Kanji, B. Sierau, M. Vrekoussis and J. Sciare, *Atmos. Chem. Phys.*, 2019, **19**, 15087–15115.
79 A. Seifert, V. Bachmann, F. Filipitsch, J. Förstner, C. M. Grams, G. A. Hoshyaripour, J. Quinting, A. Rohde, H. Vogel, A. Wagner and B. Vogel, *Atmos. Chem. Phys.*, 2023, **23**, 6409–6430.
80 Copernicus, Air Pollution at tagret cities, **https://policy.atmosphere.copernicus.eu**, accessed July 17, 2024.
81 NASA earth observatory, An atmospheric river of dust, **https://earthobservatory.nasa.gov/images/149588/an-atmospheric-river-of-dust**, accessed July 17, 2024.
82 WMO Barcelona Dust Regional Center, WMO SDS-WAS Regional Center for Northern Africa, Middle East and Europe, conducting research and providing operational products, **https://dust.aemet.es/**, accessed July 17, 2024.
83 C. Rodriguez-Navarro, F. Di Lorenzo and K. Elert, *Atmos. Chem. Phys.*, 2018, **18**, 10089–10122.

84 P. Morozzi, B. Ballarin, S. Arcozzi, E. Brattich, F. Lucarelli, S. Nava, P. J. Gómez-Cascales, J. A. G. Orza and L. Tositti, *Atmos. Environ.*, 2021, **252**, 118297.
85 E. Remoundaki, A. Bourliva, P. Kokkalis, R. E. Mamouri, A. Papayannis, T. Grigoratos, C. Samara and M. Tsezos, *Sci. Total Environ.*, 2011, **409**, 4361–4372.
86 C. Belis, O. Favez, M. Mircea, E. Diapouli, M. Manousakas, S. Vratolis, S. Gilardoni, M. Paglione, S. Decesari, G. Mocnik, D. Mooibroek, P. Salvador, S. Takahama, R. Vecchi and P. Paatero, *European guide on air pollution source apportionment with receptor models*, EUR 29816 EN, Publications Office of the European Union, Luxembourg, 2019, ISBN 978-92-76-09001-4, JRC117306, DOI: **10.2760/439106**.
87 F. Öztürk and M. Keleş, *Environ. Sci. Pollut. Res.*, 2016, **23**, 14157–14172.
88 S. Rodríguez, J. M. Prospero, J. López-Darias, M.-I. García-Alvarez, P. Zuidema, S. Nava, F. Lucarelli, C. J. Gaston, L. Galindo and E. Sosa, *Atmos. Environ.*, 2021, **246**, 118092.
89 R. A. Eldred, *J. Air Waste Manage. Assoc.*, 1997, **47**, 204–211.
90 C. N. Hewitt, *Atmos. Environ.*, 2001, **35**, 1155–1170.
91 A. M. Taiwo, R. M. Harrison and Z. Shi, *Atmos. Environ.*, 2014, **97**, 109–120.
92 Lech-Stahlwerke, Lech-Stahlwerke Company locations, **https://www.lech-stahlwerke.de/en/company/max-aicher-stiftung/locations.html**, accessed July 24, 2024.
93 F. Lucarelli, V. Barrera, S. Becagli, M. Chiari, M. Giannoni, S. Nava, R. Traversi and G. Calzolai, *Environ. Pollut.*, 2019, **247**, 802–811.
94 Rachel Carson Center, The History of Munich's Waste Management, **https://seeingthewoods.org/2019/01/08/the-history-of-munichs-waste-management/**, accessed July 24, 2024.